

Influence of argon gas bubbles and non-metallic inclusions on the flow behavior in steel continuous casting

C. Pfeiler*, M. Wu, A. Ludwig

*Christian-Doppler Laboratory for Multiphase Modeling of Metallurgical Processes, Department of Metallurgy,
University of Leoben, Franz-Josef-Street 18, A-8700 Leoben, Austria*

Received in revised form 11 July 2005

Abstract

The present study uses an Eulerian–Lagrangian approach to model the 3D turbulence (k – ϵ) flow of the steel melt (continuous phase) and the trajectories of individual non-metallic inclusions and gas bubbles (dispersed phase) in a continuous casting. The dispersed phase is considered as numerous mass-loaded particles with different classes of diameters and densities. To consider the interaction between the continuous and the dispersed phases two different methods are studied and compared. The first method, i.e. the one-way coupling, considers only the impact of the melt flow on the trajectories of the dispersed phases, while the influence of the dispersed phases on the melt flow is ignored. With the second method, namely the two-way coupling, both bidirectional influences are considered. The presented results indicate that coupling the bidirectional interactions is essential to get realistic results, especially in the presence of large gas bubbles.

© 2005 Elsevier B.V. All rights reserved.

Keywords: Turbulence; Continuous casting; Submerged entry nozzle; Inclusion; Bubble; Dispersed phase

1. Introduction

During continuous casting, non-metallic inclusions and argon gas bubbles are brought/injected into the mold. Non-metallic inclusions are originated from deoxidation, reoxidation and exogenous processes, while argon gas bubbles are intentionally injected into the nozzle to prevent clogging and to avoid attraction of ambient air [1,2]. The main concern related to the existence of non-metallic inclusions and gas bubbles is their transport in the molten pool. If the flow pattern is carefully adjusted by an optimized submerged entry nozzle (SEN) and/or optimized casting parameters, the melt flow may carry the inclusions and bubbles to the top surface, where they might be removed into the liquid slag layer. Otherwise, they will eventually be trapped by the solidification front and cause defects in the final product. The transport of inclusions and bubbles depends obviously on the flow. Therefore, great modeling efforts were made to study the melt flow in the molten pool [1,3–6] and, very recently, also to investigate directly the influence of the flow on the transport of inclusions [7–14]. Most of these publications

consider only one-way coupling, i.e. the melt flow impacts the trajectories of the inclusions, while the influence of the inclusions on the flow is ignored. However, a comprehensive model should consider bidirectional interactions between the dispersed phase and the melt flow.

Models, which are used to simulate the transport of inclusions and/or gas bubbles in liquid melts fall into three categories: (1) quasi single-phase procedure where both liquid melt and inclusions and/or bubbles are handled as one ‘mixture’ phase [9,10] (the shortcoming of this approach is that the relative motion between the different phases can only be considered approximately); (2) Eulerian two phase approaches where the dispersed inclusions and/or gas bubbles are considered as a secondary continuous phase for which an additional momentum equation is solved [8,10–12]; and (3) Eulerian–Lagrangian two-phase models where the melt flow is solved in an Eulerian framework, while the trajectories of the inclusions and/or bubbles are tracked in Lagrangian framework [7,10,13–14]. The Lagrangian method has distinct advantages over the Eulerian method in terms of formulation simplicity, ability to accommodate complicated exchange processes, computer memory requirements, and computational efforts [13]. Therefore, in the present work the Eulerian–Lagrangian method is chosen. Two different ways of coupling between the continuous and the dispersed phase

* Corresponding author. Tel.: +43 3842 402 2225; fax: +43 3842 402 2202.
E-mail address: claudia.pfeiler@mu-leoben.at (C. Pfeiler).

are compared, i.e. one-way and two-way couplings. The one-way coupling considers only the influence of the melt flow on the movement of the inclusions and/or bubbles while the back influence is ignored. The two-way coupling explicitly accounts for the bidirectional influence. The aim of this work is to study the role of coupling and its impact on the occurring melt flow and motion of inclusions and/or bubbles.

2. Model description

Mass and momentum conservation for an incompressible fluid are given by

$$\nabla \cdot \vec{u} = 0 \quad (1)$$

$$\rho \left[\frac{\partial \vec{u}}{\partial t} + (\vec{u} \cdot \nabla) \vec{u} \right] = -\nabla p + \mu_{\text{eff}} \nabla^2 \vec{u} + \vec{F} \quad (2)$$

where $\mu_{\text{eff}} = \mu_0 + \mu_t$ is the effective viscosity due to turbulence, for which the standard $k-\varepsilon$ model is used. μ_0 is the dynamic viscosity of the melt, ρ the melt density, \vec{u} is its mean velocity vector, p is the static pressure and \vec{F} is a momentum source term, which accounts for the presence of inclusions and/or bubbles. Inclusions and gas bubbles are considered as discrete secondary phases with spherical geometry disperse distributed in the melt. The trajectories of these discrete phases are computed by integrating the following equation of motion in a Lagrangian frame of reference:

$$\frac{d\vec{u}_p}{dt} = \frac{18\mu_0 C_D Re}{\rho_p d_p^2 24} [(\vec{u} + \vec{u}') - \vec{u}_p] + \frac{\vec{g}(\rho_p - \rho)}{\rho_p} \quad (3)$$

Here, \vec{u}_p is the velocity vector, d_p the diameter and ρ_p the density of the considered discrete phase. \vec{g} is the gravity vector and \vec{u}' is the vector of the fluctuating velocity components defined in Eq. (8). The trajectory of an individual discrete object is based on the forces acting as it moves through the flow. The terms on the right-hand side of Eq. (3) represent drag force and buoyancy force. For the drag coefficient, C_D , the following approach is taken [15]

$$C_D = a_1 + \frac{a_2}{Re} + \frac{a_3}{Re^2} \quad (4)$$

Here, a_1 , a_2 and a_3 are constants that apply to smooth spherical inclusions/bubbles over several ranges of Re . The relative Reynolds number, Re , is defined as

$$Re = \frac{\rho d_p |\vec{u}_p - \vec{u}|}{\mu_0} \quad (5)$$

The momentum transfer from the discrete phases towards the melt is computed by examining their momentum change as

$$\vec{F} = \sum_i^N \frac{18\mu_0 C_D Re}{\rho_p d_p^2 24} (\vec{u}_p - \vec{u}) \dot{m}_p \Delta t \quad (6)$$

Here, N is the number of inclusions and/or bubbles in a computational cell and \dot{m}_p is the mass flow rate of inclusions and/or gas bubbles.

The dispersion of the inclusions and/or bubbles due to turbulence in the melt is treated using a stochastic tracking model.

This stochastic tracking model includes the impact of instantaneous turbulent velocity fluctuations, $u'(t)$, on the trajectories. The fluctuating velocity components are discrete piecewise constant functions of time. Their random value is kept constant over an interval of time given by the rotation time of an eddy. This rotation time, τ_e , which describes the time a inclusion/bubble spent in the turbulent motion of the considered eddy, is proportional to the discrete phase dispersion rate. Larger values indicate more turbulent motion in the flow. For the $k-\varepsilon$ model, the rotation time can be expressed according to [16] as

$$\tau_e \approx 0.3 \frac{k}{\varepsilon} \quad (7)$$

The values of the fluctuations in 3D u' , v' and w' that prevail during the lifetime of the turbulent eddy are sampled by assuming that they obey a Gaussian probability distribution, so that

$$u' = \zeta \sqrt{\frac{2k}{3}}, \quad v' = \zeta \sqrt{\frac{2k}{3}}, \quad w' = \zeta \sqrt{\frac{2k}{3}} \quad (8)$$

where ζ is a normally distributed random number. The discrete phase crossing time is defined as

$$t_{\text{cross}} = -\tau \ln \left[1 - \left(\frac{L_e}{\tau |u - u_p|} \right) \right] \quad (9)$$

where τ is the discrete phase relaxation time and L_e is the eddy length scale. The inclusion/bubble is assumed to interact with the melt eddy over the smaller of the eddy rotation time and the eddy crossing time. When this time limit is reached, a new value of the instantaneous velocity is obtained by applying a new value of ζ in Eq. (8).

3. Simulation details and boundary conditions

The 3D turbulence flow in and around the SEN of a thin slab continuous casting is simulated. A trifurcated SEN is considered. Dispersed particles, i.e. non-metallic inclusions and argon gas bubbles, are injected from the top of the SEN, following the flow stream through the three nozzle ports into the mold. The geometrical and process parameters are given in Fig. 1 and Table 1. This work considers the isothermal situation. Therefore, the viscosity and density are assumed to be constant. The material data are consistent with low carbon steel at the casting temperature and are referred to literature [5]. Due to the twofold symmetry at the center planes, only a quarter of the casting is calculated. The computational domain in the liquid pool region is discretized with a structured mesh and in and around the SEN ports with an unstructured mesh. Non-conforming-mesh interfaces between the structured mesh zone and unstructured mesh zone are defined. The whole grid consists of around 500 000 cells. The time step for the simulation is chosen as small as 0.0003 s.

For the melt, a constant velocity inlet boundary condition at the top of the SEN and a constant pressure outlet condition at the bottom of the calculation domain are applied. The top surface of the liquid melt pool being in contact with the slag is assumed to be flat. Here, a free-slip condition is used. All side walls of the liquid pool are considered as ‘moving wall’ with a given

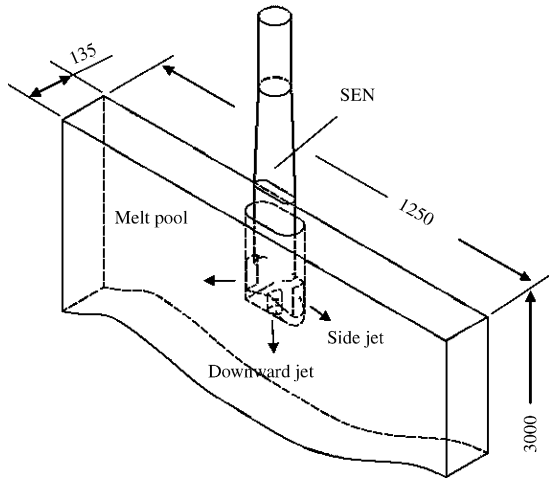


Fig. 1. Schematic representation of the physical domain of the thin slab steel caster.

constant velocity (casting speed), and a no-slip condition. The boundary condition between the melt and the SEN wall is also chosen to be no-slip, but the SEN itself is of course considered to be stationary.

Three classes of inclusions with diameters of $d = 10$, 500 and $1000 \mu\text{m}$ and one class of gas bubbles with diameter of $d = 4000 \mu\text{m}$ are defined. Each class is injected from different positions. The positions are chosen to be uniformly distributed at the inlet surface. An escape boundary condition is defined for the outlet, and a reflecting boundary for the side walls of the casting. At the top surface and at the walls in and outside the SEN, the inclusions and gas bubbles are modeled as to be caught.

Two computations one with one-way coupling and another with two-way coupling are performed. The geometry and the other conditions are chosen to be exactly equal. As mentioned above, one-way coupling means that the influence of the fluid flow on the movement of inclusions and gas bubbles is considered but not the opposite. On the other hand, the two-way coupling allows the fluid flow to be affected by the presence of the inclusions and/or bubbles.

Table 1
Geometrical and process parameters

Slab width (mm)	1250
Slab thickness (mm)	135
Slab length (mm)	3000
SEN length (mm)	832
SEN submerged depth (mm)	160
Casting speed (m/min)	2.5
Steel composition	Low carbon steel
Fluid dynamic viscosity (kg/m s)	0.00555
Fluid density (kg/m^3)	7020
Gravity acceleration (m/s^2)	9.81
Inclusion density (kg/m^3)	3700
Inclusion diameter (μm)	10, 500, 1000
Inclusion mass flow (kg/s)	$9.87\text{E}-4$
Gas density (kg/m^3)	1.6228
Gas bubble diameter (μm)	4000
Gas volume flow (l/min)	4

4. Results and discussions

4.1. Melt flow behavior

Fig. 2 shows the typical flow pattern at the central plane of the continuous casting. Here, the impact of inclusions and bubbles on the flow is not considered. The main streams of the two side jets bend upwards and build two symmetrical vortices. The jet from the middle port of the SEN flows directly downwards with a velocity as high as $v = 2.15 \text{ m/s}$. This high-speed downward jet is gradually slowed down in the lower part of the melt pool.

4.2. Motion of non-metallic inclusions and gas bubbles

Fig. 3 shows the distribution of the non-metallic inclusions and gas bubbles at different times. The gas bubbles are represented with red dots and the non-metallic inclusions with black dots. Both bubbles and inclusions are injected from the top of the SEN into the liquid melt simultaneously. The injection duration lasts only $t = 100 \text{ ms}$. Although three different size classes of the non-metallic inclusions are introduced, the simulation results show no significant difference in their motion. Therefore, in the following discussion we will not make a distinction between the different size classes.

In principle, all inclusions and bubbles follow the vertical flow stream in the SEN. They are then diverted into three branches. It is rather clear that the inclusions/bubbles following the downward jet are brought very quickly downwards, especially in the first 2 s. The inclusions/bubbles following the side jets bend upwards similar as the melt flow does. Some of them rise to the top surface (meniscus) and are 'captured by the slag', while most of them continue to follow the flow and are dispersed in the vortices. At about $t = 5 \text{ s}$, some inclusions are also branched from the side jets, bend downwards, and are gradually dispersed in the lower rolls.

The difference between the non-metallic inclusions and the gas bubbles is significant. In the SEN (see Fig. 3 for $t = 1.0288 \text{ s}$) the gas bubbles move much slower than the non-metallic inclusions. The bubbles rise quickly upwards as they get out of the nozzle side ports. Those gas bubbles are also influenced by the existing vortices, which leads to a bubble dispersion in the upper region of the melt pool. Most of the gas bubble can rise to the top surface, and are 'captured by the slag' very soon. The bubbles following the downward jet move much slower than the non-metallic inclusions. At about $t = 5 \text{ s}$, the rising speed of the bubbles has balanced with the melt flow. With time those bubbles will also rise to the upper region of the melt pool. The larger buoyancy force drives the bigger and lighter bubbles to rise much faster than the non-metallic inclusions.

4.3. Coupled simulation versus uncoupled simulation

The comparison simulations demonstrate that the two different ways of couplings do have a considerable influence on the motion of inclusions and bubbles. Both the trajectories of the inclusions/bubbles (Fig. 3) and the flow patterns (Fig. 4) are significantly different.

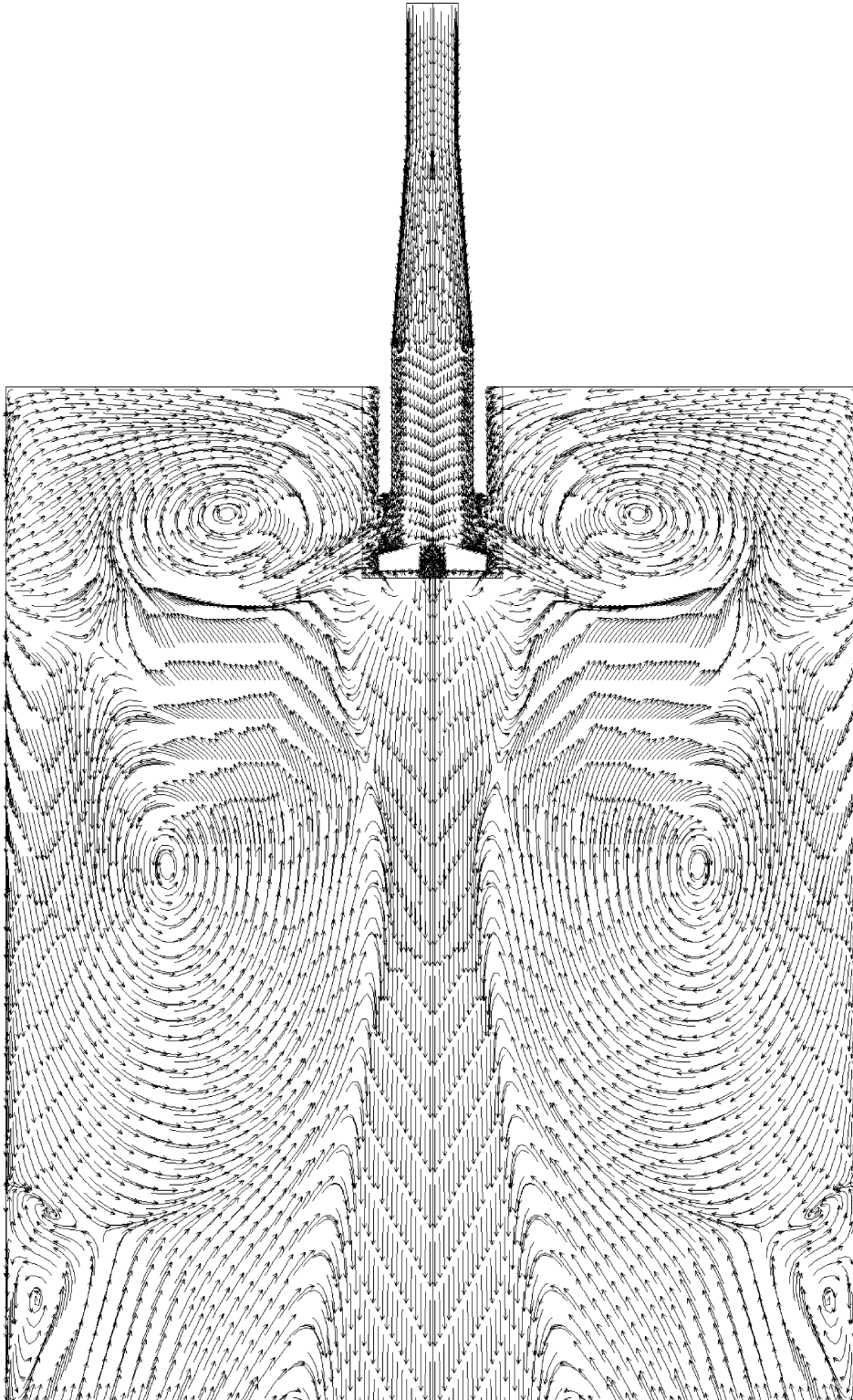


Fig. 2. Flow pattern in the plane of symmetry.

At $t = 1$ s, all the gas bubbles are still in the SEN. In the case of one-way coupling, it is found that all bubbles which are injected at the same instant move with almost the same speed. However, in the case of two-way coupling some bubbles in the center part of the nozzle move slower. For comparison, Fig. 4 shows the velocity profiles across the SEN sections for both cases at the

top surface level ('slag' level). The buoyancy force causes the bubbles to rise relative to the melt flow, and by the momentum exchange the melt flow is decelerated. If this effect on the flow is taken into account, the velocity profiles are curved in a 'W'-form. In contrast, the velocity profiles in the SEN are almost even for the case with one-way coupling.

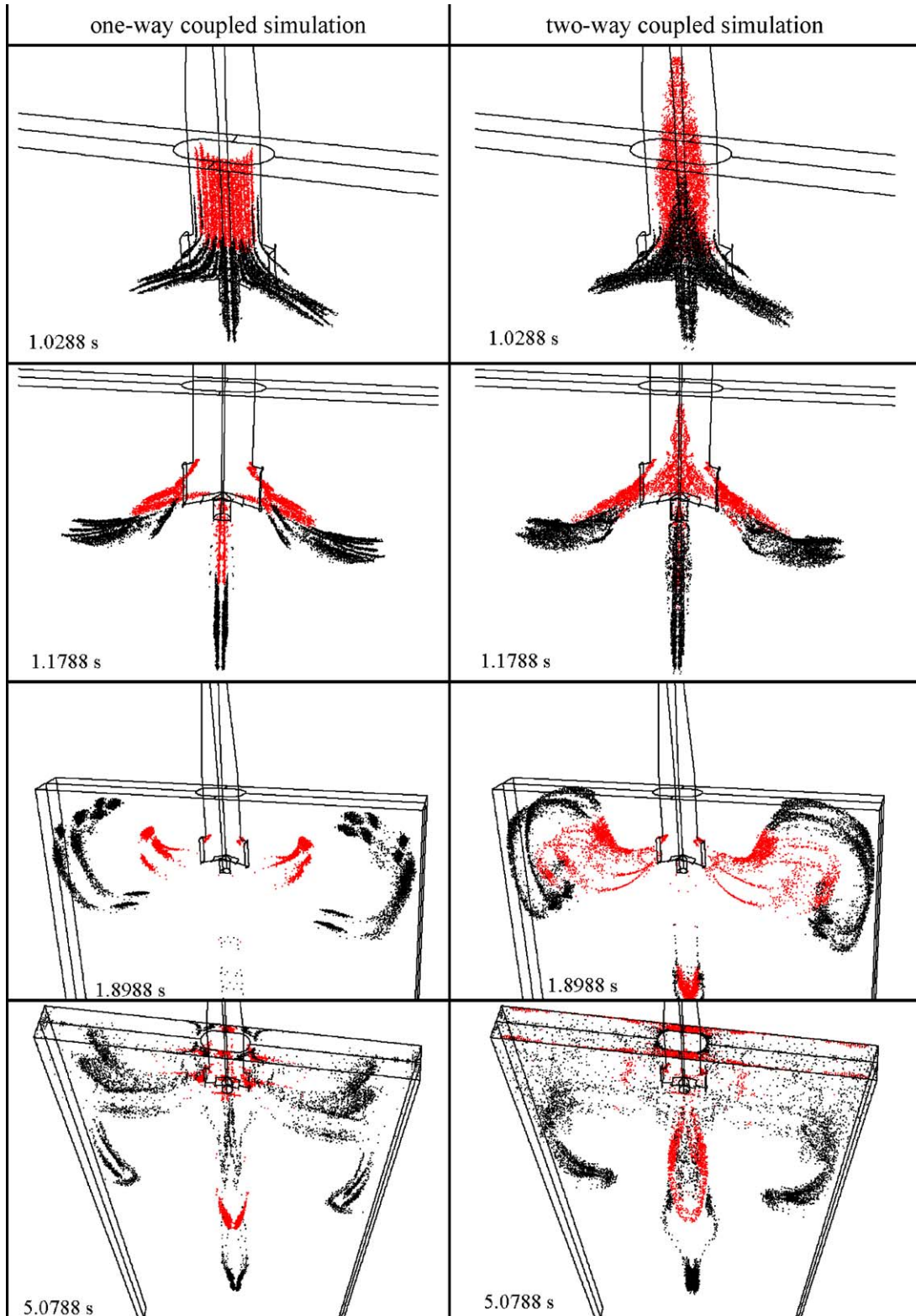


Fig. 3. Distribution of the non-metallic inclusions (black dots) and gas bubbles (red dots) at different times. Left: one-way coupled simulation; right: two-way coupled simulation.

As the inclusions and bubbles get out of the nozzle ports, the two-way coupled simulation results shows that they are more dispersedly distributed compared to the case with one-way coupling. It seems that with the consideration of momentum

exchange, the bubbles can rise more easily upward and at the end they are more dispersedly 'captured by the slag' on the top surface. We also compared the velocity patterns in the melt pool of the two cases. It is found that the macroscopic flow patterns

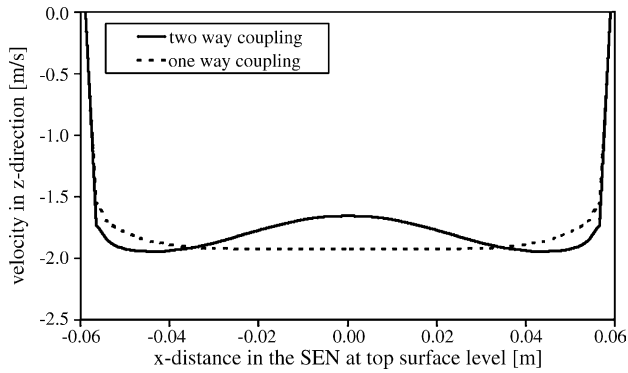


Fig. 4. Comparison of the velocity profiles in the SEN at top surface level $t = 1.0288$ s after the first inclusions/bubbles injections.

are similar, but the exact velocity magnitudes are to some extent different. Examination on corresponding details is out of the scope of this paper.

5. Conclusions

Simulations with an Eulerian–Lagrangian model for the transport of the non-metallic inclusions and gas bubbles in the SEN and the melt pool of a steel continuous caster has been performed. The comparison of a simulation which takes into account the impact of the melt flow on the motion of inclusions/bubbles with a second simulation with accounts also for the back influence, indicate that, especially for the presence of large gas bubbles, two-way coupling is essential for a proper prediction of inclusion/bubble trajectories. This conclusion is based on the following findings:

- (i) The uneven velocity profile in the nozzle causes a wider spreading of inclusions and bubbles.
- (ii) With the two-way coupling, inclusions and gas bubbles are more dispersed in the melt pool.
- (iii) The flow pattern of the steel in the melt pool is influenced by the buoyancy force acting at the gas bubbles.
- (iv) The two-way coupling shows that during gas injection the downward melt velocity in the center of the SEN is slower compared to the simulation with one-way coupling.

Acknowledgements

This work was financially supported by Austrian Christian-Doppler (CD) Research Association, VOEST-Alpine Industrieanlagenbau GmbH&Co (VAI) and RHI Refractories, in the frame of CD-Laboratory—Multiphase Simulation of Metallurgical Processes. Special thanks are due to Dr. Christian Chimani (VAI), Dr. Josef Watzinger (VAI) and D.I. Helmut Dösinger (RHI) for providing the plant data and for the discussions on industrial issues of this topic. The authors also acknowledge the technical assistance of Dr. Braun, Fluent Deutschland GmbH, Darmstadt, Germany.

References

- [1] B.G. Thomas, in: K.O. Yu (Ed.), *Modeling for Casting and Solidification Processing*, Marcel Dekker Inc., New York, 2002, pp. 499–539.
- [2] L. Zhang, B.G. Thomas, *Iron Steel Inst. Jpn. Int.* 43 (2003) 271–291.
- [3] A. Ramos-Banderas, R. Sanchez-Perez, R.D. Morales, J. Palafox-Ramos, L. Demedices-Garcia, M. Diaz-Cruz, *Metall. Mater. Trans. B* 35 (2004) 449–460.
- [4] Q. Yuan, S. Sivaramakrishnan, S.P. Vanka, B.G. Thomas, *Metall. Mater. Trans. B* 35 (2004) 967–982.
- [5] Q. Yuan, B. Zhao, S.P. Vanka, B.G. Thomas, *Steel Res. Int.* 76 (2005) 33–43.
- [6] Q. Yuan, B.G. Thomas, S.P. Vanka, *Metall. Mater. Trans. B* 35 (2004) 685–702.
- [7] Q. Yuan, B.G. Thomas, S.P. Vanka, *Metall. Mater. Trans. B* 35 (2004) 703–714.
- [8] M. Javurek, P. Gittler, R. Roessler, B. Kaufmann, H. Presslinger, *Steel Res. Int.* 76 (2005) 64–70.
- [9] B.G. Thomas, X. Huang, R.C. Sussman, *Metall. Mater. Trans. B* 25 (1994) 312–527.
- [10] D. Mazumdar, R.I.L. Guthrie, *Metall. Mater. Trans. B* 25 (1994) 308–312.
- [11] A. Mukhopadhyay, E.W. Grald, K. Dhanasekharan, S. Sarkar, J. Sanyal, *Steel Res. Int.* 76 (2005) 22–32.
- [12] M.P. Schwarz, *Appl. Math. Model.* 20 (1996) 41–51.
- [13] S.T. Johansen, F. Boysan, *Metall. Trans. B* 19 (1988) 755–764.
- [14] A. Alexiadis, P. Gardin, J.F. Domgin, *Metall. Mater. Trans. B* 35 (2004) 949–956.
- [15] S.A. Morsi, A.J. Alexander, *J. Fluid Mech.* 55 (1972) 193–208.
- [16] B.J. Daly, F.H. Harlow, *Phys. Fluids* 13 (1970) 2634–2649.